Int J Appl Earth Obs Geoinformation 91 (2020) 102153

Contents lists available at ScienceDirect

Int J Appl Earth Obs Geoinformation

journal homepage: www.elsevier.com/locate/jag

On agricultural drought monitoring in Australia using Himawari-8 geostationary thermal infrared observations

Tian Hu[a,d,*], Albert I.J.M. van Dijk[b], Luigi J. Renzullo[b], Zhihong Xu[a], Jie He[c], Siyuan Tian[b], Jun Zhou[a], Hua Li[d]

[a] Environmental Futures Research Institute, School of Environment and Science, Griffith University, Nathan, QLD 4111, Australia
[b] Fenner School of Environment and Society, Australian National University, Canberra, ACT 2601, Australia
[c] School of Life Sciences, University of Technology Sydney, Sydney, NSW 2007, Australia
[d] State Key Laboratory of Remote Sensing Science, Aerospace Information Research Institute, Chinese Academy of Sciences, Beijing 100101, China

ARTICLE INFO

Keywords:
Agricultural drought
Thermal infrared
TRI
Himawari-8

ABSTRACT

Monitoring agricultural drought effectively and timely is important to support drought management and food security. Effective drought monitoring requires a suite of drought indices to capture the evolution process of drought. Thermal infrared signals respond rapidly to vegetation water stress, thus being regarded useful for drought monitoring at the early stage. Several temperature-based drought indices have been developed considering the role of land surface temperature (LST) in surface energy and water balance. Here, we compared the recently proposed Temperature Rise Index (TRI) with several agricultural drought indices that also use thermal infrared observations, including Temperature Condition Index (TCI), Vegetation Health Index (VHI) and satellite-derived evapotranspiration ratio anomaly (Δf_{RET}) for a better understanding of these thermal infrared drought indices. To do so, we developed a new method for calculating TRI directly from the top-of-atmosphere brightness temperatures in the two split-window channels (centered around ~11 and 12 μm) rather than from LST. TRI calculated using the Himawari-8 brightness temperatures (TRI_BT) and LST retrievals (TRI_LST), along with the other LST-based indices, were calculated for the growing season (July–October) of 2015 – 2019 over the Australian wheatbelt. An evaluation was conducted by spatiotemporally comparing the indices with the drought indices used by the Australian Bureau of Meteorology in the official drought reports: the Precipitation Condition Index (PCI) and the Soil Moisture Condition Index (SMCI). All the LST-based drought indices captured the wet conditions in 2016 and dry conditions in 2019 clearly. Ranking of Pearson correlations of the LST-based indices with regards to PCI and SMCI produced very similar results. TRI_BT and TRI_LST showed the best agreement with PCI and SMCI ($r > 0.4$). TCI and VHI presented lower consistency with PCI and SMCI compared with TRI_BT and TRI_LST. Δf_{RET} had weaker correlations than the other LST-based indices in this case study, possibly because of outliers affecting the scaling procedure. The capability of drought early warning for TRI was demonstrated by comparing with the monthly time series of the greenness index Vegetation Condition Index (VCI) in a case study of 2018 considering the relatively slow response of the greenness index to drought. TRI_BT and TRI_LST had a lead of one month in showing the changing dryness conditions compared with VCI. In addition, the LST-based indices were correlated with annual wheat yield. Compared to wheat yields, all LST-based indices had a peak correlation in September. TRI_BT and TRI_LST had strong peak and average correlations with wheat yield ($r \geq 0.8$). We conclude that TRI has promise for agricultural drought early warning, and TRI_BT appears to be a good candidate for efficient operational drought early warning given the readily accessible inputs and simple calculation approach.

1. Introduction

Drought is one of the most damaging natural hazards, and has posed challenges to ecosystems and society throughout human civilization (AghaKouchak et al., 2015; Hao and Singh, 2015; Hao et al., 2017). For instance, the Millennium Drought in southeast Australia (2001 – 2009) led to a decline in irrigated rice and cotton production by 99% and 84%, respectively (van Dijk et al., 2013). Regional GDP in the southern

* Corresponding author.
E-mail address: hutian@radi.ac.cn (T. Hu).

https://doi.org/10.1016/j.jag.2020.102153
Received 11 February 2020; Received in revised form 18 April 2020; Accepted 7 May 2020
Available online 24 May 2020

Murray-Darling Basin during the Millennium Drought fell 5.7% below forecast between 2007 and 2008 consequently, accompanied by the temporary loss of 6000 jobs (Field et al., 2014). Climate projections predict that the intensity and frequency of drought will increase over many areas in the twenty-first century due to decreased precipitation or increased evaporation or both (Cai et al., 2014; Dai, 2013). Effective monitoring of developing drought at an early stage is key to drought management and mitigation (Hao et al., 2017).

Drought has been categorized as meteorological (a deficit in precipitation), hydrological (deficit in runoff, groundwater, or total water storage), agricultural (deficit in plant available water), or socio-economic (insufficient water supply for non-agricultural uses) (AghaKouchak et al., 2015; Mishra and Singh, 2010). In this study, agricultural drought is of interest due to its close relation to crop production capacity and food security (Anderson et al., 2016).

In the last few decades, numerous remote sensing indices for agricultural drought monitoring have been developed based on precipitation (*e.g.* Precipitation Condition Index, PCI; Rhee et al., 2010), vegetation thermal response (*e.g.* Temperature Condition Index, TCI; Kogan, 1995a), plant available water (*e.g.* Soil Moisture Condition Index, SMCI; Zhang and Jia, 2013), crop water requirements and actual water use (*e.g.* Evaporative Stress Index, ESI; Anderson et al., 2007), light-harvesting capacity (*e.g.* Vegetation Condition Index, VCI; Kogan, 1995b), and vegetation health (*e.g.* Vegetation Health Index, VHI; Kogan, 2001), among others. Most agricultural drought indices are either modeled by univariate analysis or bi- or multivariate analysis (AghaKouchak et al., 2015; Mishra and Singh, 2010). In univariate analyses, the anomaly of a single land surface parameter (*e.g.* precipitation or soil moisture) is usually calculated as the index. In the bi- or multivariate analyses, drought indices or variables are combined using different approaches, including the linearly weighted method (Rhee et al., 2010) and ordered weighted averaging (Jiao et al., 2019).

An effective agricultural drought monitoring system requires a suite of drought indices, and no single index can capture all the factors in the drought evolution process (Anderson et al., 2016). The evolution of agricultural drought can be categorized into four phases: latency, onset, development, and recovery (Zhang et al., 2017). In the latency phase, agricultural drought usually begins as a meteorological drought, characterized by a lack of rainfall. As the precipitation deficit continues and the root-zone soil water dries out, crop water stress occurs and drought enters the onset phase, characterized by a reduction in actual evapotranspiration and increased canopy temperature due to stress-induced stomatal closure. In the development phase, the green leaf fraction decreases due to prolonged water deficit. After precipitation occurs, drought conditions are relieved and recovery occurs. To detect agricultural drought before irreversible damage to crops, effective and timely drought monitoring at the drought onset phase is pivotal.

Land surface temperature (LST) rapidly responds to drought due to its role in the surface energy and water balance (Anderson et al., 2013). The increase of canopy temperature reflects drought as soil moisture deficit and vegetation water stress develop (McVicar and Jupp, 1998). Thus, LST-based drought indices provide independent information on drought impacts on vegetation health in comparison with precipitation-based indices typically used in drought monitoring, especially given that *in-situ* rainfall gauges are unavailable in a lot of regions and precipitation retrievals from satellite observations have coarse spatial resolutions (Anderson et al., 2015). TCI, VHI, and ESI are all LST-based drought indices. TCI and VHI are both computationally efficient given the well-developed LST and vegetation index products. However, LST is used directly in the calculation of TCI and VHI rather than in a time-differential way, which makes the indices highly sensitive to uncertainties in LST retrievals (Anderson et al., 2011; Zhao and Li, 2013). Moreover, daily or weekly composited LST products obtained from polar-orbiting satellite observations (*e.g.* MODIS) are often used in the calculation. Considering the imprecise temporal information and unfixed viewing geometry of these LST data, TCI and VHI can be greatly influenced by the temporal and directional variation of LST (Duan et al., 2012; Hu et al., 2016, 2017, 2019a,b; Rasmussen et al., 2010, 2011). ESI, developed on a clearer physical basis, has shown promise in providing early warning of drought impacts on agricultural systems (Otkin et al. 2013). It has been shown to have a higher and earlier peak in correlation with subsequent soybean yields than have leaf area index (LAI) and precipitation (Anderson et al., 2016). However, in the calculation of ESI, actual and potential evapotranspiration need to be calculated using model equations, which require ancillary meteorological data. Thus, building a robust LST-based drought index that is insensitive to LST estimation uncertainties, not influenced by temporal and directional variation of LST, and follows a simple approach that does not require ancillary climate data, would be a potentially useful addition for agricultural drought early warning capabilities.

Recently, we proposed the Temperature Rise Index (TRI), defined as the anomaly of the morning rise rate of LST (Hu et al., 2020). The principle is that the LST rise between 1.5 and 3.5 h after the sunrise is approximately linear, and that the LST rise rate (dT/dt) increases as root-zone soil moisture decreases over vegetated surfaces due to plant adaptive mechanisms (*i.e.* stomatal closure). In the method, the LST morning rise rate is obtained by fitting a linear function to the LST retrievals in the early morning, retaining regression results with a correlation coefficient $R^2 > 0.7$. In a previous study, we used LST retrievals from the geostationary Multifunction Transport Satellite-2 (MTSAT-2) instrument to calculate the index (Hu et al., 2020). Considering LST retrievals from geostationary satellite observations have fixed viewing geometry for a specific pixel, the calculation was not affected by directional LST variations. In addition, the temporal information of LST retrievals was clearly considered in the calculation. The index was demonstrated to be effective for agricultural drought early warning when compared with alternative drought indices. However, LST retrievals from geostationary satellites are not always archived, especially over long-term periods, due to the large data volume, which hinders the application of TRI in drought monitoring for a long time series. As such, calculating TRI directly from brightness temperatures would be a valuable alternative that increases the feasibility of the method and simplifies the calculation process. In addition, there are very few studies reporting recent advances in the development of LST-based agricultural drought indices. As such, a comprehensive comparison among these LST-based drought indices, including the proposed TRI (calculated from both LST and brightness temperatures), TCI, VHI and anomaly in the ratio of actual to potential evapotranspiration, is necessary for a better understanding of these indices.

In this study, we extended the calculation of TRI from using LST retrievals to using brightness temperatures directly, to facilitate the application of TRI. We employed the Himawari-8 top-of-atmosphere brightness temperatures to calculate the TRI, and compared TRI with other LST-based indices. The evaluation was implemented by comparing TRI, along with the other LST-based agricultural drought indices, with more commonly-used indices (PCI, SMCI, and VCI), and by correlating the LST-based indices with the annual wheat yield over the Australian wheatbelt growing season for the period of 2015 – 2019. The goal of this study is double-fold: first, to evaluate the method for calculating TRI directly from brightness temperatures; second, to investigate the performances of state-of-the-art LST-based drought indices.

2. Study area and data

2.1. Study area

The Australian wheatbelt was selected as the study area. This encompasses the main rainfed cropping regions in Australia, extending over 24.6 million hectares in a crescent through eastern, southern and western Australia (Fig. 1). To delineate the spatial extent of this region, the rainfed cropping pixels in the National Dynamic Land Cover Dataset

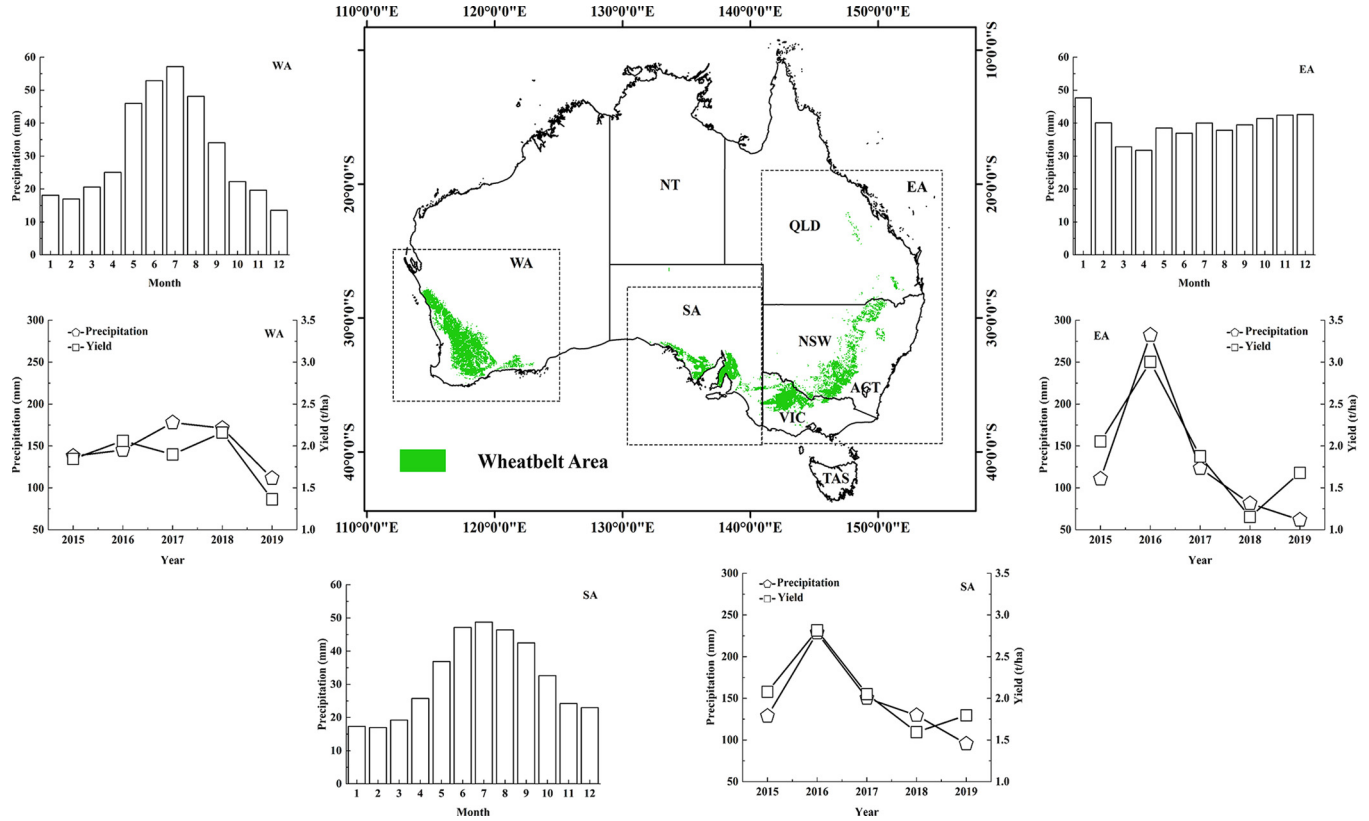

Fig. 1. Seasonality of precipitation and time series of wheat yield and rainfall for the period of 2015–2019 over the Australian wheatbelt. The green colored areas represent the Australian wheatbelt. The yield data were collected separately for three regions: Western Australia (WA), South Australia (SA), and the eastern part of the wheatbelt in New South Wales (NSW), Victoria (VIC) and Queensland (QLD). The eastern part is collectively referred to as EA hereafter. The monthly rainfall for each region was obtained by averaging the ANUClimate 1.0 precipitation data in each month between 1970 and 2016 (Hu et al., 2020). The precipitation in the time series was calculated by accumulating the BOM precipitation data (detailed in Section 2.2) in the growing season (July – October) of each year (For interpretation of the references to color in this figure legend, the reader is referred to the web version of this article).

(DLCD) v2.1 from Geoscience Australia (http://www.ga.gov.au/scientific-topics/earth-obs/accessing-satellite-imagery/landcov er) were selected. The climate over the wheatbelt varies from Temperate and Mediterranean with winter-dominant rainfall in WA and SA to subtropical with summer-dominant rainfall in EA. The wheat growing season over the wheatbelt lasts from early June to mid-November, with the peak of season at early September (Shen et al., 2018). The wheat yield is highly related with precipitation, ranging from ~1.5 t/ha in dry years to ~3 t/ha in wet years (Fig. 1).

2.2. Data

The Himawari-8 geostationary satellite is the operational meteorological satellite launched by the Japan Meteorological Agency in 2014 as the successor of MTSAT-2. It carries the highly improved Advanced Himawari Imager (AHI) onboard, located above the equator at 140.7°E (Bessho et al., 2016). The geographical coverage encompasses most of Eastern Asia, Australia, and New Zealand. The AHI has 16 observations bands (three for visible, three for near-infrared, and ten for infrared), with a temporal resolution of 10 min. The nominal spatial resolution for the split-window channels used in the study (Bands 14 and 15, centered around 11.2 and 12.4 μm) is 2 km at the sub-satellite point. The Himawari-8 data are publicly available from July 2015 onwards. In this study, the brightness temperatures in the split-window channels from July to October (covering most of the growing season) for the period 2015 – 2019 were obtained from the Australian Bureau of Meteorology (BOM), and were stored on the National Computational Infrastructure (NCI, http://nci.org.au/). To remove pixels contaminated by cloud, the cloud mask product from the cloud property product suite of BOM was obtained, which provides the clear-sky probability in a pixel-wise method. The pixels with clear-sky probabilities > 0.9 were deemed as cloud-free and used to calculate TRI. From 2018, the cloud mask product was not available from BOM. For this period, we used the algorithm developed by Shang et al. (2017) based on the Himawari-8 multispectral observations instead. The LST morning rise rate was calculated using the Himawari-8 split-window brightness temperatures, and TRI was obtained as the anomaly of LST morning rise rate. To compare between TRI obtained from brightness temperatures and LST retrievals, the hourly Himawari-8 LST product for the study period was obtained from the Copernicus Global Land Service (https://land.copernicus.eu/global/products/lst). The Himawari-8 LST retrievals were produced using the Generalized Split-Window (GSW) algorithm from the two adjacent split-window channels and provided at about 0.045° regular grids (Freitas et al., 2013). The hourly LST product was retrieved by using full disk scans closest to the reference time noted in the filename (about ± 10 min apart from the reference time).

Daily gridded precipitation data for 2015 – 2019 were obtained from BOM (http://www.bom.gov.au/water/landscape). The data are produced from approximately 6500 rain gauge stations and interpolated to 0.05° × 0.05° regular grids using a robust topography-resolving analysis method (Jones et al., 2009). Deciles or percentiles of precipitation are used mostly as operational drought indices by BOM in official reports (http://www.bom.gov.au/climate/drought/). Here, we used the anomaly of precipitation to remain consistent with other indices used in the evaluation (calculated as the anomaly of specific climatic or vegetation condition parameters).

Root-zone soil moisture data were obtained from the Australian Water Resources Assessment-Landscape (AWRA-L) version 6.0 model

(van Dijk, 2010; van Dijk and Renzullo, 2011; http://www.bom.gov.au/water/landscape/), representing the percentage of available water content in the top 1 m of the soil profile. The root-zone soil moisture data are provided on a regular grid with a spatial resolution of 0.05°.

The monthly composite Normalized Difference Vegetation Index (NDVI) data (MYD13C2 v6) of Moderate Resolution Imaging Spectroradiometer (MODIS) were obtained from the Land Processes Distributed Active Archive Center (LPDAAC; https://lpdaac.usgs.gov). The spatial resolution of the NDVI product is 0.05°. VCI was calculated using the monthly NDVI data. The daily MODIS temperature product (MYD11A1 v6) was also obtained from the LPDAAC with 1-km spatial resolution. The temperature retrievals were derived using the generalized split-window algorithm (Wan and Dozier, 1996). The temperature product was reprojected and resampled to 0.05° regular grids using the Application for Extracting and Exploring Analysis Ready Samples (AppEEARS) tool (https://lpdaacsvc.cr.usgs.gov/appeears/). Considering Terra/MODIS thermal bands (Bands 27–30) have a crosstalk issue, only Aqua/MODIS products were used here. TCI was calculated using the daytime LST data and composited to monthly time scale (Kogan, 1995a). VHI was obtained as the simple average of VCI and TCI by assuming an equal contribution of VCI and TCI (Kogan, 2001).

Estimates of the ratio of actual over potential evapotranspiration (f_{RET}) with a spatial resolution of 0.05° were used to calculate the f_{RET} anomaly (Δf_{RET}). These data were an intermediate output of the global thermal-based ESI product (https://gis1.servirglobal.net/data/esi/) and were provided directly by the developers (C. Hain and M. Anderson, pers. comm., 2019). They are derived from thermal LST retrievals from the MODIS polar-orbiting satellite observations, used as input into the Atmosphere-Land Exchange Inverse (ALEXI) model to estimate actual evapotranspiration (Anderson et al., 2015). Potential evapotranspiration was calculated using the Penman-Monteith (PM) equation (Anderson et al., 2015). Δf_{RET} was integrated over 4-week periods to approximate the monthly composites. We did not use the ESI data provided online directly because the ESI product on the SERVIR GLOBAL website was calculated by transforming the composited f_{RET} to a "z-score" using the mean and standard deviation. This anomaly calculation method is different from that used for the other indices. In addition, the period baseline for the anomaly calculation of the ESI product (2001–2018) was different from the study period here. To avoid these impacts on the comparison among indices, Δf_{RET} was calculated following the same method as for other indices, scaled using the maximum and minimum values. The data developers note that the f_{RET} may be more prone to outliers than some of the other indices evaluated, and this should be considered in the interpretation.

Wheat yield data for each state were obtained from the Australian crop report by the Department of Agriculture and Water Resources (http://www.agriculture.gov.au/abares). Here, the yield data were collected separately for WA, SA, and EA.

3. Methodology

3.1. Index calculation

3.1.1. TRI calculation

Given that LST change in the early morning is quasi-linear (Duan et al., 2012; Hu et al., 2020), LST (denoted T) at time t can be expressed as:

$$T(t) = At + B \tag{1}$$

where A is dT/dt, and B is the intercept. The temperature difference (ΔT) between time t and a reference time t_r is hence given by:

$$\Delta T(t) = T(t) - T(t_r) = A(t - t_r) = A\Delta t. \tag{2}$$

In Eq. 2, ΔT is a linear function of the time difference (Δt), with the same slope (A) as the LST morning rise. Thus, dT/dt can be obtained by regressing the slope in Eq. 2.

Coll and Caselles (1997) developed a split-window algorithm that considered the atmospheric and emissivity effects separately by using different terms in a quadratic equation:

$$T = T_{11} + a(T_{11} - T_{12}) + b(T_{11} - T_{12})^2 + c + B(\varepsilon, W) \tag{3}$$

where T_{11} and T_{12} are the top-of-atmosphere brightness temperatures centered around 11 and 12 μm, respectively; a, b, and c are the atmospheric coefficients independent of surface properties, among which a and b are functions of view zenith angle (θ), c is a constant; the term B is a function of surface emissivity and atmospheric column water vapor content (W)

$$B(\varepsilon, W) = (\alpha_0 + \alpha_1 W)(1 - \varepsilon) - (\beta_0 + \beta_1 W + \beta_2 W^2)\Delta\varepsilon \tag{4}$$

where $\varepsilon = (\varepsilon_{11} + \varepsilon_{12})/2$ is the mean emissivity for the two bands centered around 11 and 12 μm, $\Delta\varepsilon = \varepsilon_{11} - \varepsilon_{12}$ is the emissivity difference, α_0, α_1, β_0, β_1, and β_2 are constants.

Niclòs et al. (2011) implemented the quadratic split-window equation (Eq. 3) on observations from the Spinning Enhanced Visible and Infrared Imager (SEVIRI) onboard the geostationary METEOSAT Second Generation 2 (MSG-2) satellite. They evaluated the split-window algorithm using *in-situ* measurements in Eastern Spain and reported that the temperature estimates retrieved using the proposed algorithm had absolute biases around 0.2 K and root-mean-square error (RMSE) within 1 K, with higher accuracy on average by 0.6 K than the operational SEVIRI LST product. Furthermore, Duan et al. (2014) pointed out that the variation of the term B during the entire day was negligible. The variation is expected to be much smaller for the period between 1.5 and 3.5 h after the sunrise in view of the short time span. We conducted an analysis to confirm that the temporal variation of the term B is negligible over the continent Australia in the early morning. Under the assumption that the temporal variation of emissivity is negligible during the 2-h period in the early morning, the variation of B caused by the change of W is quantified as

$$\Delta B = (\alpha_1(1 - \varepsilon) - \beta_1\Delta\varepsilon)(W_t - W_{t_r}) - \beta_2\Delta\varepsilon(W_t^2 - W_{t_r}^2) \tag{5}$$

where W_t and W_{t_r} are the atmospheric water vapour contents at time t

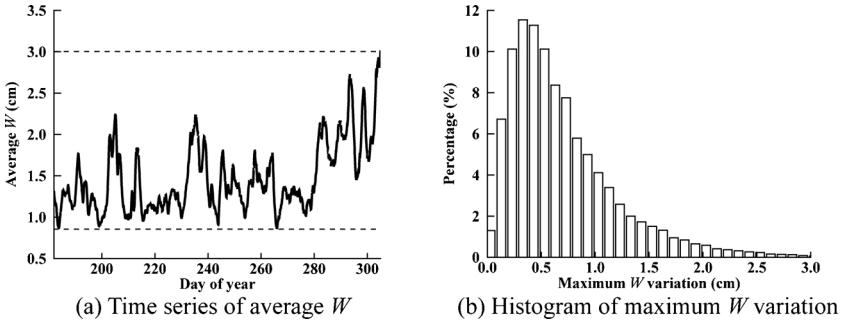

(a) Time series of average W (b) Histogram of maximum W variation

Fig. 2. Variation of average atmospheric water vapor content over the Australian continent. (a) Time series of water vapor content averaged over the continent Australia in 2015. The time series starts from July 1st 2015. (b) Histogram of maximum W variation in the entire day during the growing season in 2015. W was obtained from the National Centers for Environmental Prediction (NCEP) hourly 0.2° × 0.2° atmospheric profile product (https://rda.ucar.edu/datasets/ds094.1/).

and the reference time t_r, respectively. Based on the W variation in 2015 over Australia (Fig. 2), the maximum of $W_t - W_{t_r}$ was assumed to be 0.5 cm (maximum W variation during the entire day with the highest percentage in the histogram), and the maximum of $W_t + W_{t_r}$ 6 cm (double of the maximum W during the growing season). Niclòs et al. (2011) listed the coefficient values in Eq. 4 for MSG-2 SEVIRI observations, which were 54.68 K (α_0), -4.578 K cm^{-1} (α_1), 91.96 K (β_0), -15.16 K cm^{-1} (β_1), and 0.601 K cm^{-2} (β_2), respectively. Two extreme emissivity settings representing sand ($\varepsilon = 0.96$, $\Delta\varepsilon = -0.02$) and vegetation ($\varepsilon = 0.99$, $\Delta\varepsilon = 0$) were used. As such, the variations of the term B caused by W variation for sand and vegetation were -0.21 K and -0.02 K, respectively. Considering the similar spectral response functions of the split-window channels for MSG-2 SEVIRI and Himawari-8, we expect that the variation of B for Himawari-8 is close to that for MSG-2 SEVIRI. The variations of the term B in other years had the same magnitude based on our analysis. Therefore, the term B was assumed to be a constant during the two-hour period.

Based on the developments above, the temperature difference can hence be calculated as

$$\Delta T(t) = T_{b14}(t) + a(T_{b14}(t) - T_{b15}(t)) + b(T_{b14}(t) - T_{b15}(t))^2 - (T_{b14}(t_r) + a(T_{b14}(t_r) - T_{b15}(t_r)) + b(T_{b14}(t_r) - T_{b15}(t_r))^2) \quad (6)$$

where T_{b14} and T_{b15} are the brightness temperatures in Himawari-8 Bands 14 (~11.2 μm) and 15 (~12.4 μm), respectively. The coefficients a and b can be calculated as

$$a(\theta) = a_0 + a_1(\sec(\theta) - 1) \quad (7)$$

$$b(\theta) = b_0 + b_1(\sec(\theta) - 1) \quad (8)$$

where a_0, a_1, b_0, and b_1 are constants. To regress these coefficients for Himawari-8, we compiled a simulation data set with the latest Thermodynamic Initial Guess Retrieval (TIGR) database (Chedin et al., 1985; Chevallier et al., 1998). The MODTRAN 5.2 atmospheric radiative transfer model was used to simulate the top-of-atmosphere brightness temperatures. The atmospheric conditions were described using the 946 clear-sky TIGR profiles (Hu et al., 2017). Surface skin temperatures were extracted from the bottom layer temperatures in the TIGR profiles and modified by seven increment values (-6, -2, 1, 3, 5, 8 and 12 K). Thirteen θ values were considered, ranging from nadir to 80°. Then, $a(\theta)$ and b(θ) were calculated at different angles through regression analysis between the simulated $T - T_{b14}$ and $T_{b14} - T_{b15}$ by considering $\varepsilon = 1$ and $\Delta\varepsilon = 0$ (Coll and Caselles, 1997). Fig. 3 shows the regression results of a and b as functions of $\sec(\theta) - 1$. By using the least-square regression, a and b can be expressed using two segmental linear functions:

$$a(\theta) = \begin{cases} 0.0047 - 0.7939(\sec(\theta) - 1), \theta < 62.5° \\ -2.6556 + 1.4983(\sec(\theta) - 1), \theta \geq 62.5° \end{cases} \quad (9)$$

$$b(\theta) = \begin{cases} 0.0641 + 0.0328(\sec(\theta) - 1), \theta < 62.5° \\ 0.1458 - 0.0374(\sec(\theta) - 1), \theta \geq 62.5° \end{cases} \quad (10)$$

Therefore, the temperature difference between time t and t_r can be calculated using the brightness temperatures in Bands 14 and 15 based on Eq. 6. In the calculation, we selected the reference time as the earliest clear-sky observation time in the 2-h period between 1.5 and 3.5 h after the sunrise.

The flowchart for TRI calculation is illustrated in Fig. 4. During the 2-h period after the sunrise, there were 13 potential observations (brightness temperatures in Bands 14 and 15) from Himawari-8. Thus, 12 values of temperature difference (ΔT) could be attained at most. The cloud masking was implemented by selecting pixels with clear-sky probabilities > 0.9 based on the Himawari-8 cloud mask product. The cropping pixels were obtained by selecting the ones classified as rainfed cropping land in the DLCD product. dT/dt was obtained by fitting a linear function between temperature difference and time difference (Eq. 2). In the fitting process, only results with a coefficient of determination (R^2) > 0.7 and with no fewer than 3 samples were retained to mitigate propagation from errors such as residual cloud and measurement noise. The dT/dt grids were then reprojected and resampled to 0.05° to match the other data. The calculated daily dT/dt was composited to fill the cloud-covered areas, producing a spatially largely continuous result. In addition, the compositing process made the calculated dT/dt compatible with other data in temporal resolution. The compositing was implemented by calculating an unweighted average of dT/dt within a certain period as follows:

$$dT/dt(i, j, p, y) = \frac{1}{N}\sum_{n=1}^{N} dT/dt(i, j, n, y) \quad (11)$$

where $dT/dt(i, j, p, y)$ is the composite for period p, year y and i, j grid location, $dT/dt(i, j, n, y)$ is the value on day n, and N is the number of days with accepted fitting results during the composite interval. Here, dT/dt was composited within a 1-month interval. TRI was then calculated as a scaled index:

$$TRI = \frac{dT/dt_{p,max} - dT/dt_{p,y}}{dT/dt_{p,max} - dT/dt_{p,min}} \quad (12)$$

where $dT/dt_{p,max}$ and $dT/dt_{p,min}$ are the maximum and minimum dT/dt for period p among all the years, respectively, and $dT/dt_{p,y}$ is dT/dt for compositing period p and year y.

In comparison, TRI was also calculated from the processed Himawari-8 LST retrievals. The calculation process of dT/dt is the same as mentioned above, except that dT/dt was obtained by linear regression between LST retrievals and time between 1.5 and 3.5 h after the sunrise (Eq. 1; Hu et al., 2020). The calculated dT/dt was resampled to 0.05° and composited to 1-month time scale. TRI was then obtained as the anomaly of dT/dt among all the years.

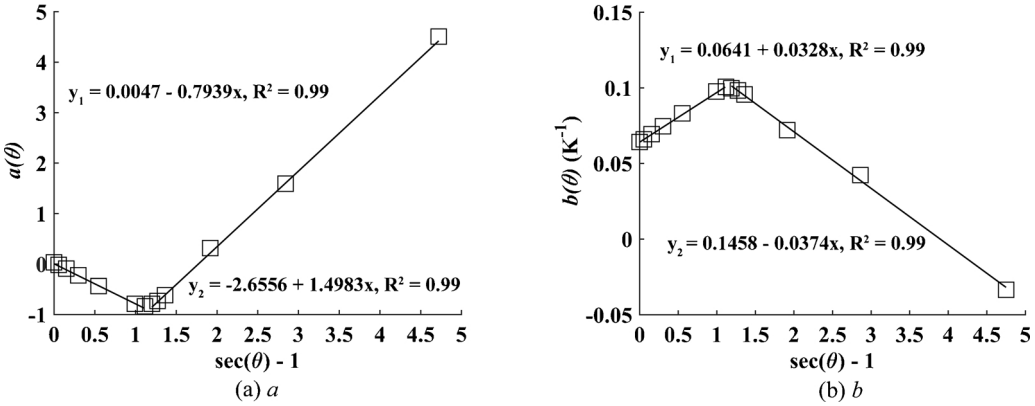

Fig. 3. Coefficients a and b as segmental linear functions of $\sec(\theta) - 1$. θ is the view zenith angle. The coefficients of determination in all cases are > 0.9.

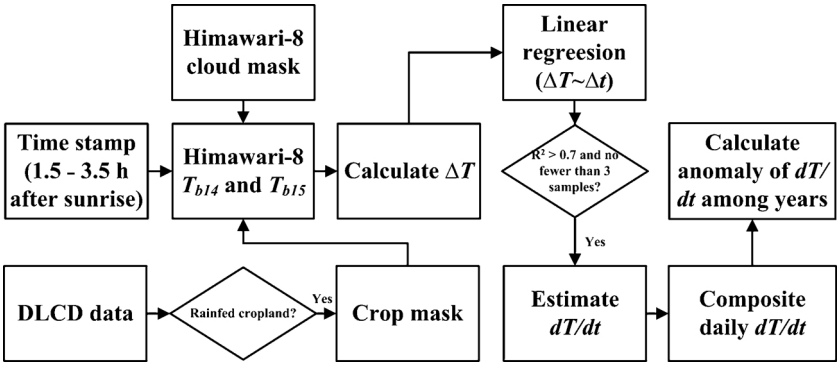

Fig. 4. Flowchart for TRI calculation.

Table 1
Formulas for alternative agricultural drought indices. P and SM represent precipitation and soil moisture, respectively. The maximum and minimum values for the variables are obtained for the same integrative period among all the years between 2015 and 2019.

Drought index	Formula
PCI	$(P - P_{min})/(P_{max} - P_{min})$
VCI	$(NDVI - NDVI_{min})/(NDVI_{max} - NDVI_{min})$
SMCI	$(SM - SM_{min})/(SM_{max} - SM_{min})$
TCI	$(LST_{max} - LST)/(LST_{max} - LST_{min})$
VHI	0.5VCI + 0.5TCI
Δf_{RET}	$(f_{RET} - f_{RET,min})/(f_{RET,max} - f_{RET,min})$

3.1.2. Calculation of other indices

Formulas for the other indices are shown in Table 1. A time lag exists between meteorological drought manifested by PCI and agricultural drought (Rhee et al., 2010). The 3-month seasonal time scale for precipitation was reported to be appropriate for agricultural drought (Rhee et al., 2010; Rouault and Richard, 2003; Hu et al., 2020). Thus, PCI integrated within 3-month timescale was used in the evaluation. It is noted that Anderson et al. (2011, 2013, 2016) calculated the ESI by transforming f_{RET} into a standardized anomaly of "z-score", normalized to a mean zero and a standard deviation of one. For consistency with the treatment of the other indices, in this study f_{RET} was scaled between 0 and 1 using the maximum and minimum values for the composite intervals in the period 2015–2019 here. This scaled f_{RET} is referred to as Δf_{RET} to distinguish from the normalized ESI.

3.2. Evaluation

The drought severity levels indicated by the different indices were unified by classifying the anomaly values (between 0 and 1, with a step of 0.1) into ten categories. Vegetation water availability increases as the indices change from 0 to 1. In the official drought report released monthly by BOM (http://www.bom.gov.au/climate/drought/), anomalies of precipitation and soil moisture in the root zone from the AWRA-L model are used as indicators of drought. To stay in line with the drought monitoring of BOM, the same precipitation and root-zone soil moisture data were used here and the anomalies of them (*i.e.* PCI and SMCI) were regarded as the standards to evaluate the drought indices.

The evaluation was conducted in three steps. First, we compared the drought patterns depicted by the LST-based indices with those depicted by PCI and SMCI for the growing season among different years. The time series of LST-based drought indices were compared with that of VCI to demonstrate the early warning capability in a case study considering the relatively slow response of the greenness index to changes in vegetation water availability (Anderson et al., 2013). At the second stage, spatial and temporal correlation analyses were conducted between the LST-based indices and PCI and SMCI. Indices were compared via spatial correlation across the wheatbelt for each month (July – October) for 2015–2019 and via temporal correlation throughout the whole study period (20 samples) for each location over the wheatbelt. Pearson correlation coefficient (r) was used to quantify the consistency between the LST-based drought indices and PCI and SMCI. At the third stage, the correlations between wheat yield and the LST-based indices were analyzed by monthly timestep. For each month from July to October, 15 samples (three regions over the wheatbelt for 5 years) were collected for each LST-based index and used for correlation analysis. The capabilities for different LST-based indices to reflect drought impact on wheat yield were evaluated.

4. Result and analysis

4.1. Drought patterns and time series depicted by different indices

Droughts patterns for the growing season during the period of 2015–2019 are shown in Fig. 5. Drought patterns among these years are strongly variable. According to the annual climate statement from BOM (http://www.bom.gov.au/climate/drought/), 2016 was the 15th-wettest year for Australia, with an area-average rainfall of 544.99 mm, well above the 1961–1990 average of 465.2 mm. 2019 was the warmest and driest year on record for Australia, with nationally-averaged rainfall 40% below the average. The contrasting drought patterns in 2016 and 2019 are demonstrated by the standard indices PCI and SMCI clearly. The spatial distribution patterns of PCI and SMCI are quite similar in all years, except that SMCI shows drier conditions in 2016 for the central part of the wheatbelt in WA than PCI. All LST-based indices capture the wet conditions in 2016 and dry conditions in 2019. The spatial patterns embodied by all the LST-based indices are consistent over southeast Australia. However, some inconsistencies exist over southwest Australia.

Compared with PCI, TRI_BT and TRI_LST show better consistency than the other LST-based indices overall, with average $r > 0.5$ (Table 2). For 2015, PCI shows wet conditions over the northern edge of the wheatbelt in WA. The similar wetness conditions are identified by TRI_BT and TRI_LST over this region, but the other LST-based indices present relatively drier conditions. In particular, Δf_{RET} shows the driest condition over a larger proportion of WA, in agreement with the weak spatial correlation between PCI and Δf_{RET} in 2015 ($r = 0.15$). PCI over a large proportion of the central WA is in the range of 0.6–0.7 in 2016. TRI_BT and TRI_LST capture this spatial pattern. Whereas, all the other LST-based indices show wetter conditions than PCI, being in the range of 0.9–1.0. For 2017, PCI shows pronounced dryness over most of SA and EA. Δf_{RET} presents similar drought patterns over these regions, with best consistency with PCI ($r = 0.6$). For 2018 and 2019, the LST-based indices have similar drought patterns, capturing the contrasting wetness conditions between WA and the other regions in 2018 and the widespread dryness in 2019. r between PCI and LST-based indices in

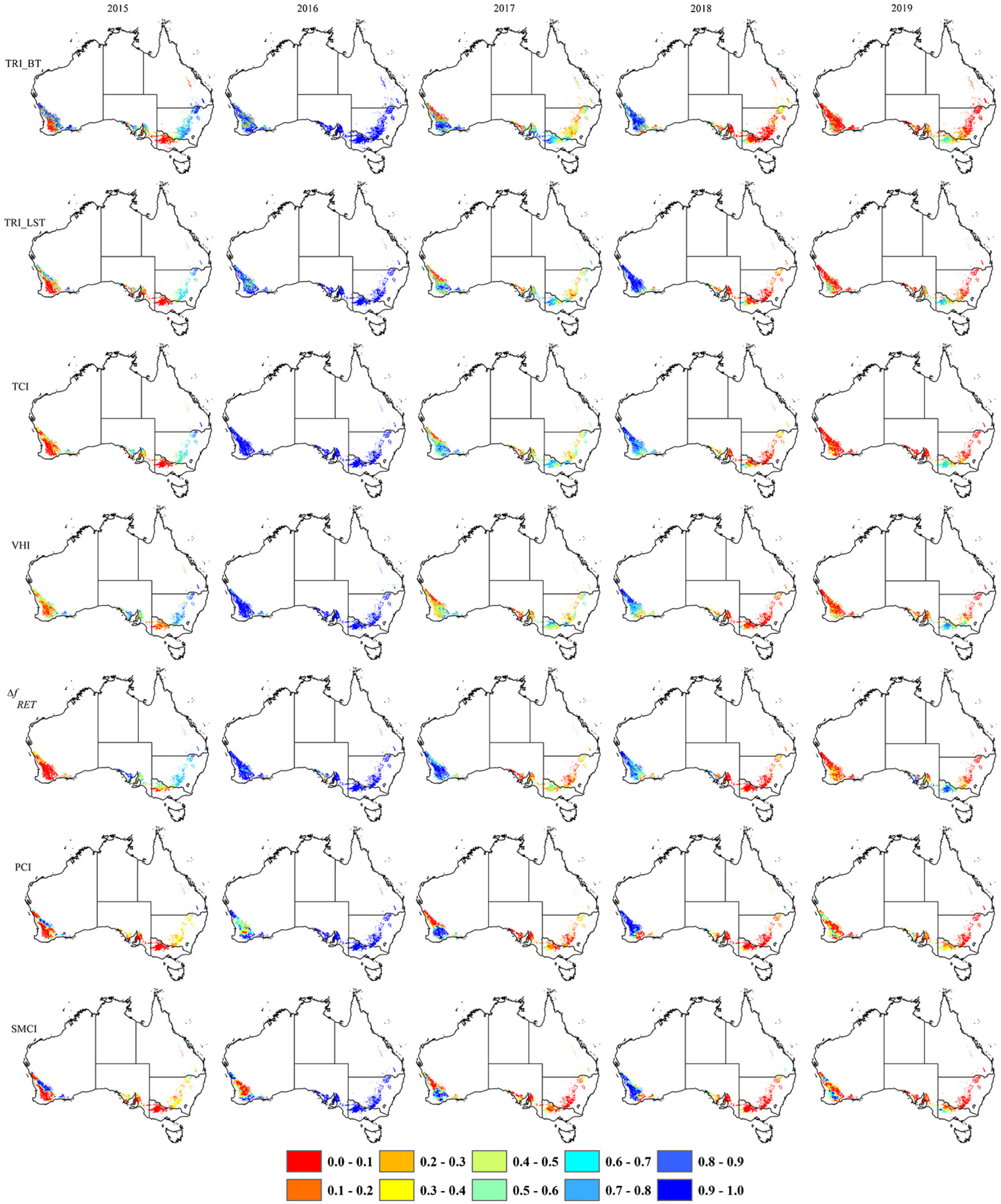

Fig. 5. Drought patterns for the period of July to October observed by multiple agricultural drought indices. Vegetation water availability increases as the indices change from 0 to 1. TRI_LST and TRI_BT represent TRI calculated from Himawari-8 LST retrievals and brightness temperatures, respectively. Given the time lag between precipitation-based indices and agricultural drought indices, PCI was calculated for the period of May to October based on the 3-month seasonal timescale.

Table 2
Correlation of LST-based drought indices with PCI and SMCI for the growing period in different years, respectively. The largest r in each year is noted with an asterisk superscript.

Drought index	2015	2016	2017	2018	2019	mean
PCI used as standard						
TRI_BT	0.59	0.58*	0.55	0.83	0.34	0.58
TRI_LST	0.63*	0.56	0.53	0.84	0.40*	0.59*
TCI	0.54	0.09	0.60*	0.84	0.34	0.48
VHI	0.52	−0.11	0.34	0.87*	0.26	0.38
Δf_{RET}	0.15	0.05	0.60*	0.84	0.33	0.39
SMCI used as standard						
TRI_BT	0.53	0.60*	0.50	0.84	0.29	0.55
TRI_LST	0.55*	0.60*	0.47	0.85*	0.41*	0.58*
TCI	0.40	0.10	0.48	0.82	0.34	0.43
VHI	0.36	−0.08	0.22	0.82	0.22	0.31
Δf_{RET}	0.05	0.05	0.59*	0.84	0.16	0.34

2018 and 2019 are around 0.85 and 0.35, respectively.

Similar to PCI, SMCI has better consistency with TRI_BT and TRI_LST than with the others, with average $r > 0.5$. The ranking of LST-based indices in terms of r with SMCI is identical to that obtained by regarding PCI as the standard, with TRI_BT and TRI_LST having the strongest r and VHI having the weakest r.

Overall, TRI_BT and TRI_LST have the best performance. The drought patterns shown by TRI_BT and TRI_LST are in strong agreement, which is also emphasized by the similar r with PCI and SMCI. The other LST-based indices also have good performance in some years, *e.g.* Δf_{RET} in 2017 and VHI in 2018, but are not as consistent as TRI_BT and TRI_LST in all the five years.

A case study of changing dryness condition for the growing season is presented in Fig. 6. The standard SMCI indicates a drying trend from July to September for most of WA. The dry condition is relieved in October due to the above average rainfall. TRI_BT and TRI_LST presents this changing drought patterns clearly, with deteriorating drought conditions until September. In contrast, VCI shows a delayed response to the changing dryness condition, in agreement with the findings reported by Hu et al. (2020). The drying trend is presented from August to October by VCI, with a time lag of one month compared with TRI. The mitigation of drought conditions in October is not shown by VCI due to the lagged response of the greenness index.

4.2. Spatial correlation analysis

Fig. 7 demonstrates the temporal variability in spatial correlations obtained between LST-based indices and the standards PCI and SMCI at monthly time scale. All correlations exhibit inter-annual variations. The change trends are similar for all the correlations, but with different magnitudes in temporal variation. r for TRI_BT and TRI_LST are more consistent in the time series, with less variation over different years.

Judging from the correlation with PCI, TRI_BT and TRI_LST have the best performance with average $r > 0.4$. TRI_BT and TRI_LST have

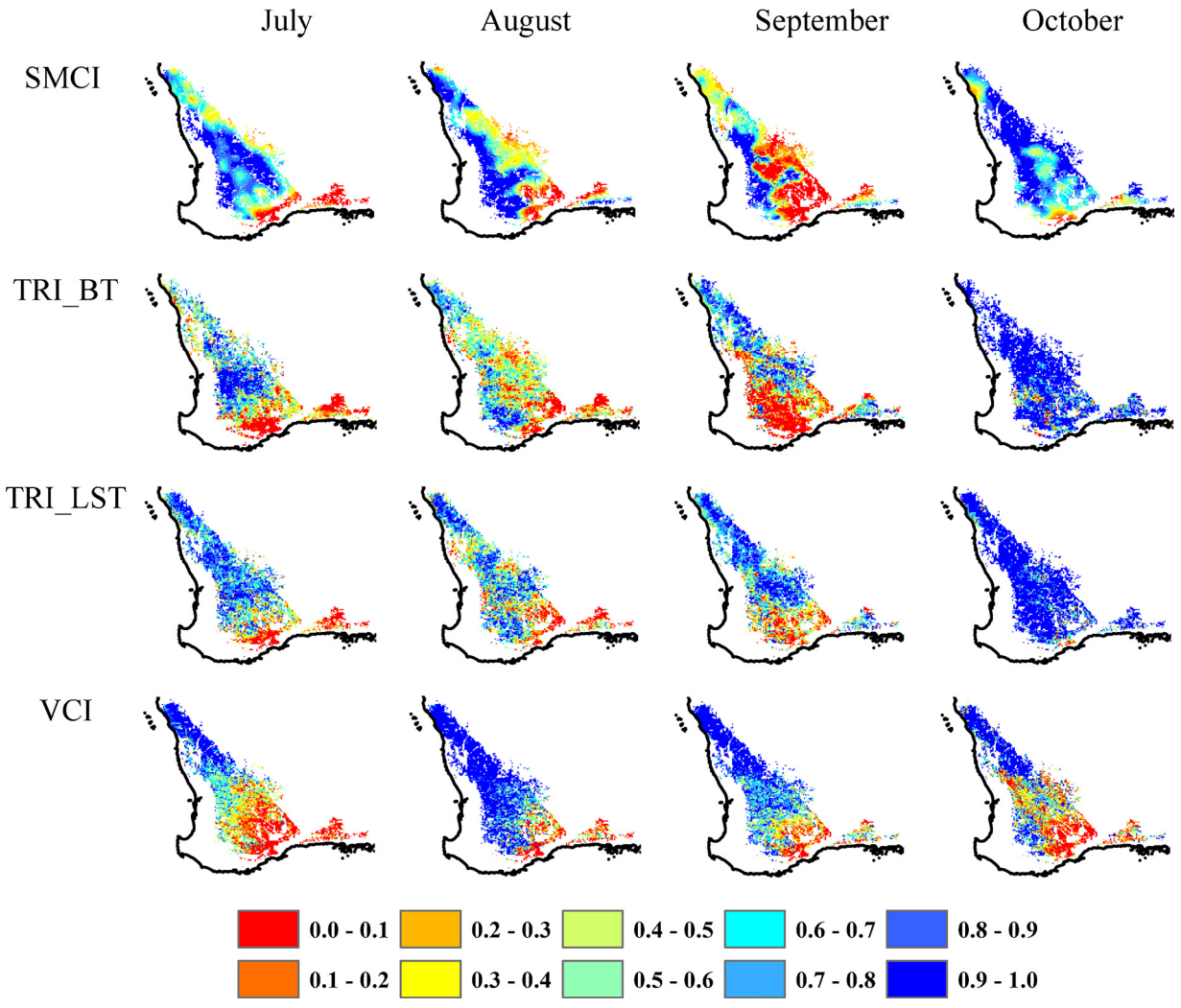

Fig. 6. Temporal evolution of drought indices from July to October 2018 in WA.

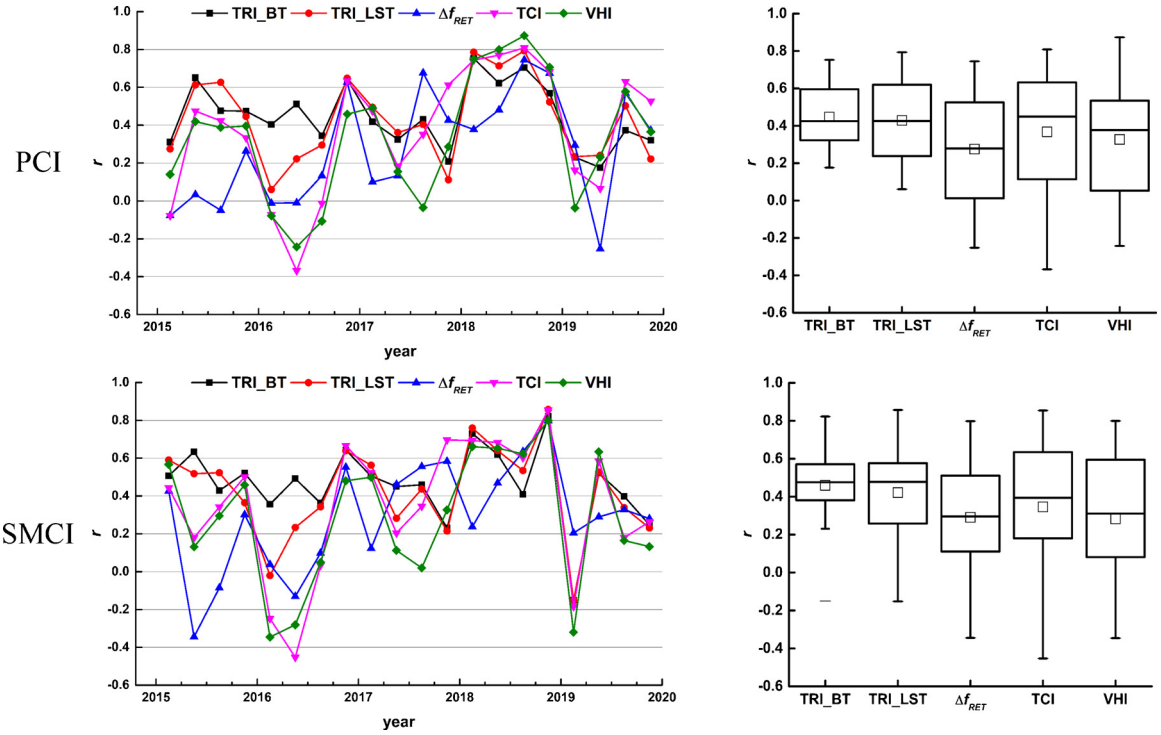

Fig. 7. Time series and statistical distributions of spatial correlation coefficients (*r*) between the LST-based and standard indices at monthly time scale. *r* was calculated using all the pixel pairs over the wheatbelt for each month from July to October in the period of 2015–2019. The square in the box plot represent the mean of each index.

similar performances, with TRI_BT having a slightly stronger *r* than TRI_LST. TCI and VHI have relatively weaker *r* with PCI compared with TRI_BT and TRI_LST, and they have average $r < 0.4$. Δf_{RET} has the weakest *r* with PCI among the LST-based indices with an average *r* of about 0.3. The maximum *r* for different indices are quite close (~0.8), but the minimum vary pronouncedly. The minimum *r* for TRI_BT and TRI_LST are greater than 0, but those for the other indices reach below −0.2.

In comparison with SMCI, TRI_BT and TRI_LST have the best agreement, both strongly correlated with SMCI ($r > 0.4$), and TRI_BT has a slightly greater mean and median of *r*. Correlations of the other indices with SMCI are weaker (means < 0.4).

The ranking of LST-based indices in terms of *r* with PCI is identical to that obtained by comparing to SMCI, suggesting that TRI_BT and TRI_LST have the best performance. Considering PCI and SMCI are widely used in agricultural drought monitoring, TRI appear to be a promising indicator of drought.

4.3. Temporal correlation analysis

The spatial distribution of temporal correlation is shown in Fig. 8. Southeast Australia generally shows high *r* (> 0.8) in all maps. Southwest Australia has lower *r* with some maps having $r < 0$. The means of the temporal correlations averaged across the wheatbelt for all the correlations are generally > 0.5.

Overall, temporal correlations give almost identical rankings to those based on monthly spatial correlations. Judging from the correlations with both PCI and SMCI, TRI_BT and TRI_LST have the best performance, with the highest average *r* overall. Different from the slightly better performance of TRI_BT than TRI_LST in the spatial correlation analysis, the average *r* of TRI_LST is marginally better than that of TRI_BT.

4.4. Correlation with crop yield

In general, the LST-based indices have strong correlation with wheat yield ($r > 0.5$ in most cases; Table 3). All indices have the strongest correlation with wheat yield occurring in September, with $r > 0.8$. This is consistent with the time for the peak of season in the wheat growing phenology. TRI_LST and VHI have the strongest peak *r* (0.89) among all LST-based indices. TRI_BT and TRI_LST have similar peak *r*, with TRI_LST having slightly stronger average *r*. Judging by the average correlation with wheat yield among all the months, TRI_LST and VHI show better performances, followed by TRI_BT. TCI also shows a strong average *r*. Δf_{RET} shows the weakest average correlation with wheat yield.

5. Discussion

5.1. Factors influencing the comparison

Because of the limited temporal coverage of the Himawari-8 satellite, the analysis could only be conducted for the five-year period 2015–2019. However, by combining the operational Himawari-8 satellite and the backup-satellite Himawari-9 launched in November 2016, the Himawari-8/9 should provide continuous observations over Australia until 2029. By combining a constellation of geostationary satellites including MTSAT-1R/2 and Himawari-8/9, the proposed method for calculating TRI directly from brightness temperatures can be applied to the observations from these satellites and provide agricultural drought monitoring over Australia for more than 20 years.

In the evaluation of LST-based indices, only a selection of indices that are widely used and applicable at global scale were considered. We did not include the crop water stress index (CWSI; Jackson et al., 1981) and Normalized Difference Temperature Index (NDTI; McVicar and Jupp, 2002) considering their similar connotations to f_{RET}, representing the ratio of actual evapotranspiration to potential evapotranspiration. The Temperature – Vegetation Dryness Index (TVDI; Sandholt et al.,

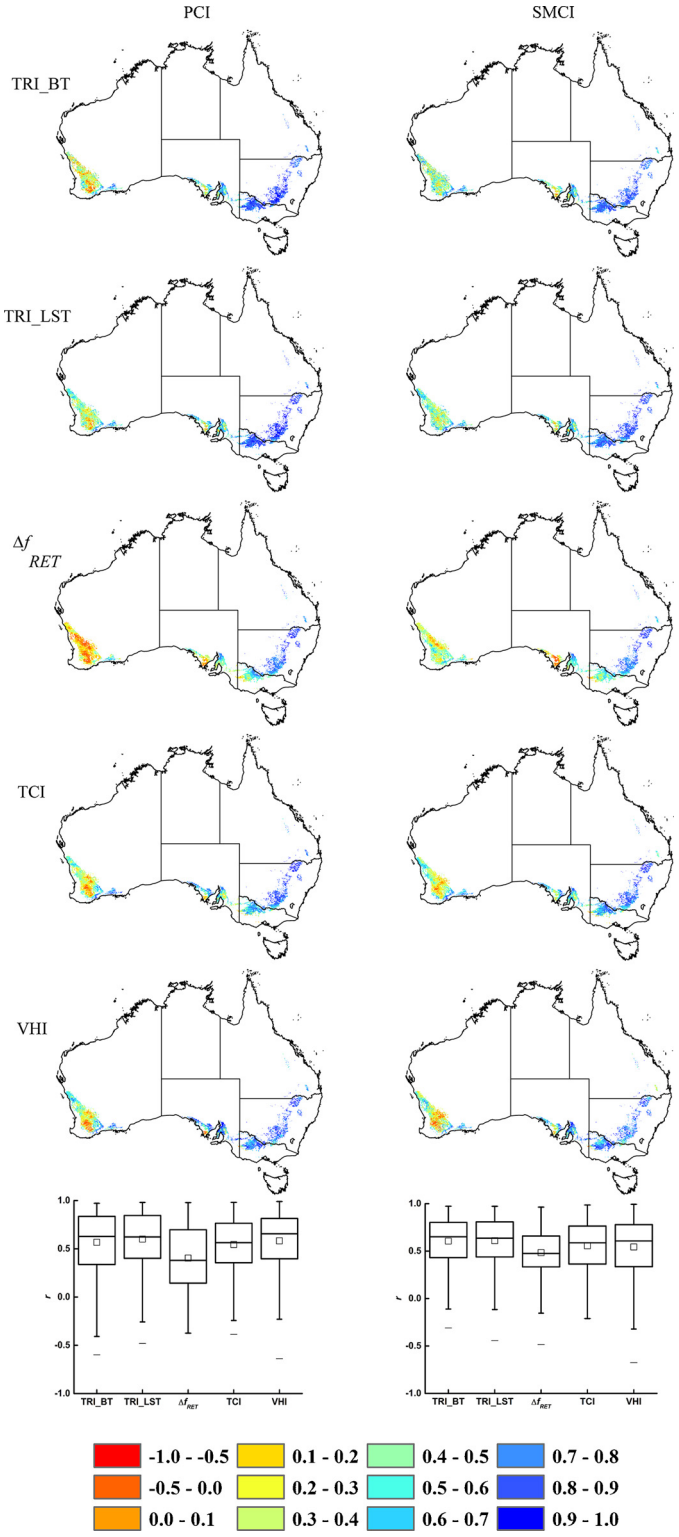

Fig. 8. Spatial distributions and statistics of temporal correlation coefficients (r) between LST-based and alternative indices. r at each pixel was calculated using the 20 pairs from July to October between 2015 and 2019.

2002) developed based on the empirical parameterization of the relationship between LST and NDVI was not analyzed since the triangular or trapezoid space in the scatterplot of LST and NDVI is normally constructed using all the samples in the study area, which makes TVDI more suitable for monitoring drought at local or regional scale. Moreover, the requirements of a full range of water variability cannot always be satisfied.

Table 3
Pearson correlation between crop yield and the LST-based drought indices. Correlations are significant ($p < 0.05$) in all cases except those noted with an asterisk superscript. The largest r among the 4 months for each index is shown in italics typeface.

Month	TRI_BT	TRI_LST	Δf_{RET}	TCI	VHI
July	0.78	0.70	0.52	0.73	0.78
August	0.75	0.85	0.19*	0.67	0.75
September	*0.87*	*0.89*	*0.82*	*0.87*	*0.89*
October	0.79	0.83	0.61	0.74	0.88
Mean	0.80	0.82	0.54	0.75	0.83

We used the DLCD land cover map for 2015 for the five-year study period from 2015 to 2019 due to the unavailability of DLCD map after 2015. However, we compared the land cover change over the Australian wheatbelt area from 2010 to 2015 based on the DLCD map in each year and found that the changes are negligible. Thus, we assume that the land cover map in 2015 is applicable throughout.

Although the study area here was the wheat cropping zone in Australia, we speculate that the evaluation results for the LST-based drought indices should be similar in other arid and semi-arid areas considering the analogue sensitivity of thermal signals to vegetation water availability in water-limited conditions.

5.2. Comparison between TRI_BT and TRI_LST

In the calculation of TRI_BT, the threshold of clear-sky possibility (0.9) used for cloud masking is the same as that used in the estimation of Himawari-8 LST from the Copernicus Global Land Service (https://land.copernicus.eu/global/products/lst) to mitigate the influence of cloud contamination on the inter-comparison between TRI_LST and TRI_BT.

Compared with dT/dt calculated using Himawari-8 brightness temperature, dT/dt calculated using Himawari-8 LST retrievals have better daily and monthly spatial coverage. The average coverage of daily and monthly dT/dt maps obtained using LST retrievals are 44% and ~100%, respectively, and 40% and 98% for those obtained using brightness temperatures. The average percentage of pixels with $R^2 > 0.7$ and > 0.9 among clear-sky pixels is also higher for dT/dt maps obtained using LST retrievals (97% and 92%, respectively), compared with those obtained using brightness temperatures (88% and 80%, respectively). These better statistics obtained using Himawari-8 LST retrievals may be because fewer samples (1-h temporal resolution) were collected for the linear regression in this case. Consequently, the selection criterion ($R^2 > 0.7$) was more easily satisfied.

Fig. 9 shows a comparison between the spatial distribution of dT/dt calculated from the Himawari-8 brightness temperatures and LST retrievals. The spatial distribution of dT/dt calculated using brightness temperatures and LST retrievals are highly consistent. The difference in dT/dt spatial pattern for 2015 is slightly larger than for other years, which is reflected in the difference distribution in the corresponding histogram. The peak of the histogram for 2015 is located between −1 and 0.5 K/h, peaks for other years are between −0.5 and 0 K/h. Compared with dT/dt calculated using LST retrievals, dT/dt calculated using brightness temperatures are generally lower.

In line with the consistent dT/dt calculated using brightness temperatures and LST retrievals, TRI_BT and TRI_LST showed similar performance. TRI_BT had a relatively better agreement with PCI and SMCI than TRI_LST in the spatial correlation analysis. However, TRI_LST showed marginally stronger r in the temporal correlation analysis. Considering r in the temporal correlation analysis was calculated based on only 20 samples, r in the spatial analysis may be more representative of the consistency between indices. Regarding the correlation with wheat yield, TRI_BT and TRI_LST had similar peak r, but TRI_LST did

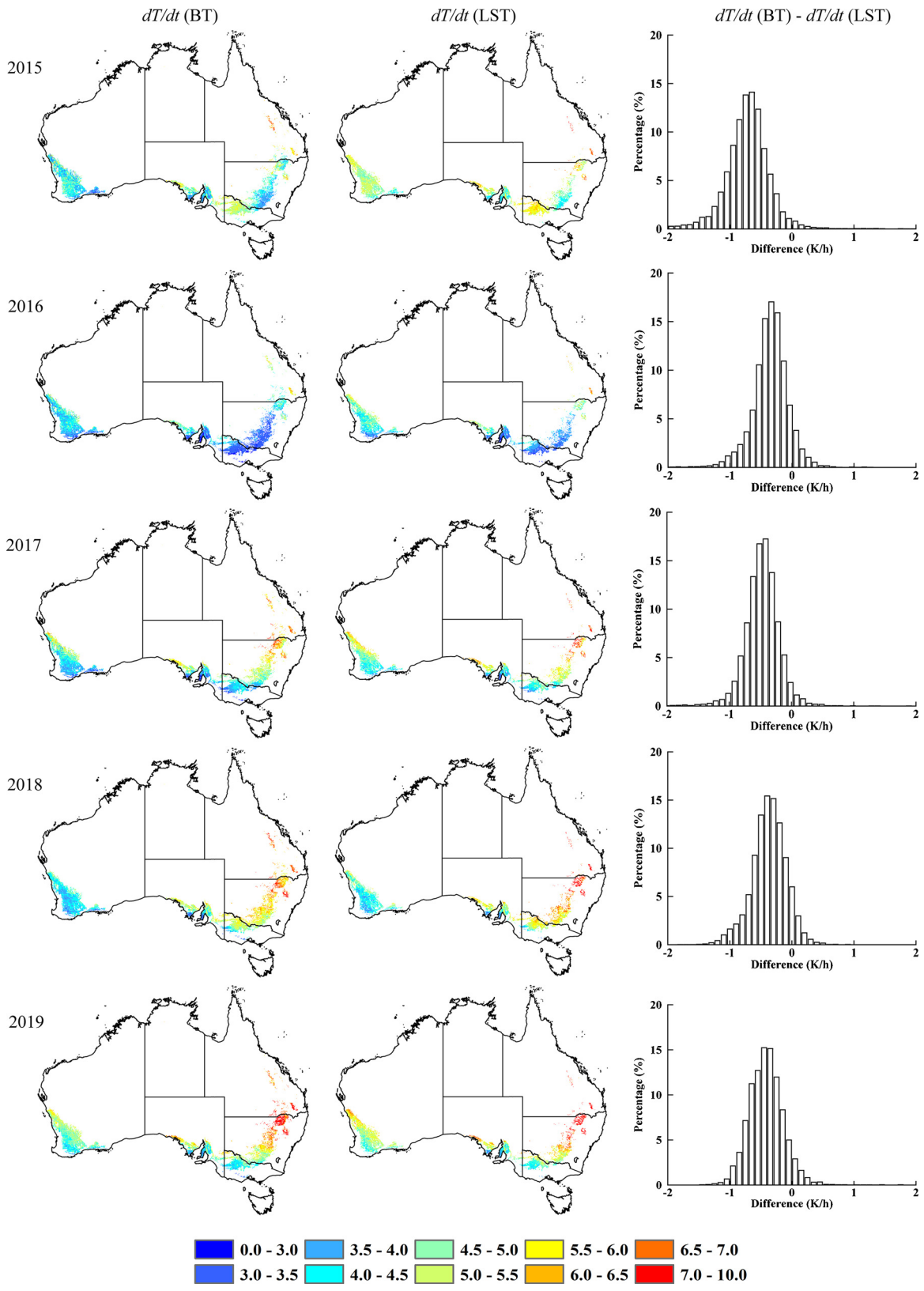

Fig. 9. Comparison between LST morning rise rates calculated using Himawari-8 brightness temperatures and LST retrievals. LST morning rise rates were composited for the entire growing period each year. The LST morning rise rates were not divided evenly considering few samples were < 3 K/h or > 7 K/h.

show a stronger average *r*.

Despite the similar performances of TRI_BT and TRI_LST, the requirements for TRI_BT calculation are much easier to meet. It can be implemented using brightness temperatures in the split-window channels directly without requiring LST retrievals. This is a potential advantage because LST retrievals from geostationary satellite data are rarely archived for long due to the data storage requirements. Even though the Copernicus Global Land Service portal provides global LST

Table 4
Pearson correlation with wheat yield for Δf_{RET} calculated using different methods. The largest r among the 4 months for each method is shown in italics typeface. $< f_{RET} >$ is the average f_{RET} and std is the standard deviation of f_{RET}.

Month	$(f_{RET} - f_{RET,min})/(f_{RET,max} - f_{RET,min})$	$(f_{RET} - < f_{RET} >)/\text{std}$	f_{RET}	$f_{RET} - < f_{RET} >$
July	0.52	0.50	0.40	0.59
August	0.19	0.20	0.23	0.26
September	*0.82*	*0.85*	*0.89*	*0.90*
October	0.61	0.63	0.62	0.72
Mean	0.54	0.55	0.54	0.62

coverage estimated from observations by a constellation of geostationary satellites (MSG, GOES, and MTSAT/Himawari-8), LST retrievals are only provided from October 2010 onwards. By contrast, TRI_BT can be used to monitor agricultural drought for a long period only if observations in the split-window channels from geostationary satellites are available.

In this study, TRI_BT was reprojected and aggregated to 0.05° to enable comparison with other indices. However, TRI_BT can also be obtained at the original spatial resolution (2 km with geostationary projection in the case of Himawari-8), providing greater detail in drought condition mapping.

5.3. Influence of anomaly calculation method

In our study, we used the maximum and minimum values to scale the indices considering the definitions of multiple indices such as PCI, SMCI and TCI, as well as the comparability among different indices. In such a scaling scheme, Δf_{RET} showed a worse performance compared with other LST-based indices. However, it is noted that the anomaly calculation method could have influenced the performance of Δf_{RET} considering the f_{RET} is derived from the modeled actual and potential evapotranspiration, and may be more likely to contain outliers compared to the other semi-empirical indices (M. Anderson and C. Hain, pers. comm., 2019). To investigate this, we evaluated the anomalies calculated using maximum and minimum values and those calculated using mean and standard deviation following Anderson et al. (2015). We found that the LST-based indices had similar performances under these two scaling schemes when spatiotemporally compared with the standards PCI and SMCI, with TRI_LST and TRI_BT performing the best and Δf_{RET} having a worse performance than the others. We further compared the correlation with wheat yield for Δf_{RET} calculated by different methods (Table 4). The unscaled anomaly ($f_{RET} - < f_{RET} >$) had the strongest r with wheat yield in all the months, and showed the strongest peak correlation ($r = 0.9$) among all LST-based indices. Yang et al. (2018) also found that, at least for short time series, an unscaled anomaly can provide more robust (as well as more easily interpreted) results because of uncertainties in the scaling factors or limits from a limited sample population. Thus, a detailed comparison between TRI and Δf_{RET} needs to be conducted when the Himawari-8 observations are available for a longer period ($>$ 10 years).

6. Conclusion

Thermal infrared remote sensing is widely used in agricultural drought monitoring at the early stage due to the rapid response of thermal signals to vegetation water stress. The present study extended the calculation of TRI from using LST retrievals to using brightness temperatures directly, and compared TRI with other LST-based agricultural drought indices over the Australian wheatbelt. The main conclusions reached are as follows:

1. Judging from the drought patterns for the growing season, TRI_BT and TRI_LST showed better consistency with the standard indices PCI and SMCI than the other LST-based indices overall, with $r > 0.5$. Compared with the greenness index VCI, TRI_BT and TRI_LST responded to the changing dryness condition at least 1 month earlier.

2. In both the spatial and temporal correlation analysis, TRI_BT and TRI_LST showed the best performance, both in good agreement with PCI and SMCI ($r > 0.4$ in spatial analysis and > 0.5 in temporal analysis). Δf_{RET} showed the weakest spatial correlation, possibly because of outliers affecting the scaling procedure. TRI_BT and TRI_LST showed similar performances in the analysis, but input requirements for TRI_BT calculation are much easier to meet.

3. all LST-based indices had a correlation peak in the same month, occurring in September. TRI_LST and VHI had the strongest overall peak correlations with wheat yield ($r = 0.89$), marginally higher than TRI_BT ($r = 0.87$).

4. When Δf_{RET} was calculated using a non-scaled simple method (subtracting the mean from f_{RET}), it showed a peak correlation with wheat yield ($r = 0.90$) higher than the other LST-based indices. Given that Δf_{RET} appears sensitive to the anomaly calculation method due to outliers in the estimated evapotranspiration, a detailed comparison between TRI and Δf_{RET} needs to be conducted when the thermal infrared observations from the Himawari-8 satellite are available for a longer period.

CRediT authorship contribution statement

Tian Hu: Conceptualization, Methodology, Data curation, Writing - original draft. **Albert I.J.M. van Dijk:** Writing - review & editing. **Luigi J. Renzullo:** Writing - review & editing. **Zhihong Xu:** Supervision. **Jie He:** Data curation. **Siyuan Tian:** Data curation. **Jun Zhou:** Supervision. **Hua Li:** Data curation.

Declaration of competing interest

The authors declare that they have no known competing financial interests or personal relationships that could have appeared to influence the work reported in this paper.

Acknowledgements

The authors wish to extend their gratitude to Dr. Martha Anderson (USDA) and Dr. Christopher Hain (NASA), who provided the f_{RET} data and assistance with their interpretation. This study was supported by Open Fund of State Key Laboratory of Remote Sensing Science, Aerospace Information Research Institute, Chinese Academy of Sciences (Grant No. OFSLRSS201903).

References

AghaKouchak, A., Farahmand, A., Melton, F.S., Teixeira, J., Anderson, M.C., Wardlow, B.D., Hain, C.R., 2015. Remote sensing of drought: progress, challenges and opportunities. Rev. Geophys. 53, 452–480.

Anderson, M.C., Norman, J.M., Mecikalski, J.R., Otkin, J.A., Kustas, W.P., 2007. A climatological study of evapotranspiration and moisture stress across the continental United States based on thermal remote sensing: 1. Model formulation. J. Geophys. Res. Atmos. 112.

Anderson, M.C., Hain, C., Wardlow, B., Pimstein, A., Mecikalski, J.R., Kustas, W.P., 2011. Evaluation of drought indices based on thermal remote sensing of evapotranspiration over the continental United States. J. Clim. 24, 2025–2044.

Anderson, M.C., Hain, C., Otkin, J., Zhan, X., Mo, K., Svoboda, M., Wardlow, B., Pimstein, A., 2013. An intercomparison of drought indicators based on thermal remote sensing

and NLDAS-2 simulations with US Drought Monitor classifications. J. Hydrometeorol. 14, 1035–1056.
Anderson, M.C., Zolin, C.A., Hain, C.R., Semmens, K., Yilmaz, M.T., Gao, F., 2015. Comparison of satellite-derived LAI and precipitation anomalies over Brazil with a thermal infrared-based Evaporative Stress Index for 2003–2013. J. Hydrol. (Amst.) 526, 287–302.
Anderson, M.C., Zolin, C.A., Sentelhas, P.C., Hain, C.R., Semmens, K., Yilmaz, M.T., Gao, F., Otkin, J.A., Tetrault, R., 2016. The Evaporative Stress Index as an indicator of agricultural drought in Brazil: an assessment based on crop yield impacts. Remote Sens. Environ. 174, 82–99.
Anderson, M., Hain, C., 2019. Personal Communication.
Bessho, K., Date, K., Hayashi, M., Ikeda, A., Imai, T., Inoue, H., Kumagai, Y., Miyakawa, T., Murata, H., Ohno, T., 2016. An introduction to Himawari-8/9—japan's new-generation geostationary meteorological satellites. J. Meteorol. Soc. Jpn. 94, 151–183.
Cai, W., Borlace, S., Lengaigne, M., Van Rensch, P., Collins, M., Vecchi, G., Timmermann, A., Santoso, A., McPhaden, M.J., Wu, L., 2014. Increasing frequency of extreme El Niño events due to greenhouse warming. Nat. Clim. Change 4, 111–116.
Chedin, A., Scott, N.A., Wahiche, C., Moulinier, P., 1985. The improved initialization inversion method: a high resolution physical method for temperature retrievals from satellites of the TIROS-N series. J. Clim. Appl. Meteorol. 24, 128–143.
Chevallier, F., Chéruy, F., Scott, N.A., Chédin, A., 1998. A neural network approach for a fast and accurate computation of a longwave radiative budget. J. Appl. Meteorol. 37, 1385–1397.
Coll, C., Caselles, V., 1997. A split-window algorithm for land surface temperature from advanced very high resolution radiometer data: validation and algorithm comparison. J. Geophys. Res. Atmos. 102, 16697–16713.
Dai, A., 2013. Increasing drought under global warming in observations and models. Nat. Clim. Change 3, 52–58.
Duan, S.-B., Li, Z.-L., Wang, N., Wu, H., Tang, B.-H., 2012. Evaluation of six land-surface diurnal temperature cycle models using clear-sky in situ and satellite data. Remote Sens. Environ. 124, 15–25.
Duan, S.-B., Li, Z.-L., Tang, B.-H., Wu, H., Tang, R., 2014. Direct estimation of land-surface diurnal temperature cycle model parameters from MSG–SEVIRI brightness temperatures under clear sky conditions. Remote Sens. Environ. 150, 34–43.
Field, C., Barros, V., Mach, K., Mastrandrea, M., 2014. IPCC (intergovernmental panel on climate change) (2014) impacts, adaptation, and vulnerability. Contribution of Working Group II to the Fifth Assessment Report of the Intergovernmental Panel on Climate Change. Cambridge University Press, Cambridge, United Kingdom and New York, NY USA.
Freitas, S.C., Trigo, I.F., Macedo, J., Barroso, C., Silva, R., Perdigão, R., 2013. Land surface temperature from multiple geostationary satellites. Int. J. Remote Sens. 34, 3051–3068.
Hao, Z., Singh, V.P., 2015. Drought characterization from a multivariate perspective: A review. J. Hydrol. 527, 668–678.
Hao, Z., Yuan, X., Xia, Y., Hao, F., Singh, V.P., 2017. An overview of drought monitoring and prediction systems at regional and global scales. Bull. Am. Meteorol. Soc. 98, 1879–1896.
Hu, T., Du, Y., Cao, B., Li, H., Bian, Z., Sun, D., Liu, Q., 2016. Estimation of upward longwave radiation from vegetated surfaces considering thermal directionality. IEEE Trans. Geosci. Remote. Sens. 54, 6644–6658.
Hu, T., Cao, B., Du, Y., Li, H., Wang, C., Bian, Z., Sun, D., Liu, Q., 2017. Estimation of surface upward longwave radiation using a direct physical algorithm. IEEE Trans. Geosci. Remote. Sens. 55, 4412–4426.
Hu, T., Renzullo, L.J., Cao, B., van Dijk, A.I.J.M., Du, Y., Li, H., Xu, Z., Zhou, J., Liu, Q., 2019a. Directional variation in surface emissivity inferred from the MYD21 product and its influence on estimated surface upwelling longwave radiation. Remote Sens. Environ. 228, 45–60.
Hu, T., Li, H., Cao, B., van Dijk, A.I.J.M., Renzullo, L.J., Xu, Z., Zhou, J., Du, Y., Liu, Q., 2019b. Influence of emissivity angular variation on land surface temperature retrieved using the generalized split-window algorithm. Int. J. Appl. Earth Obs. Geoinf. 82, 101917.
Hu, T., Renzullo, L.J., van Dijk, A.I.J.M., He, J., Tian, S., Xu, Z., Zhou, J., Liu, T., Liu, Q., 2020. Monitoring agricultural drought in Australia using MTSAT-2 land surface temperature retrievals. Remote Sens. Environ. 236, 111419.
Jackson, R.D., Idso, S.B., Reginato, R.J., Pinter Jr, P.J., 1981. Canopy temperature as a crop water stress indicator. Water Resour. Res. 17, 1133–1138.
Jiao, W., Tian, C., Chang, Q., Novick, K.A., Wang, L., 2019. A new multi-sensor integrated index for drought monitoring. Agric. For. Meteorol. 268, 74–85.
Jones, D.A., Wang, W., Fawcett, R., 2009. High-quality spatial climate data-sets for Australia. Aust. Meteorol. Oceanogr. J. 58, 233–248.
Kogan, F.N., 1995a. Application of vegetation index and brightness temperature for drought detection. Adv. Space Res. 15, 91–100.
Kogan, F.N., 1995b. Droughts of the late 1980s in the United States as derived from NOAA polar-orbiting satellite data. Bull. Am. Meteorol. Soc. 76, 655–668.
Kogan, F.N., 2001. Operational space technology for global vegetation assessment. Bull. Am. Meteorol. Soc. 82, 1949–1964.
McVicar, T.R., Jupp, D.L.B., 1998. The current and potential operational uses of remote sensing to aid decisions on drought exceptional circumstances in Australia: a review. Agric. Syst. 57, 399–468.
McVicar, T.R., Jupp, D.L.B., 2002. Using covariates to spatially interpolate moisture availability in the Murray–darling Basin: a novel use of remotely sensed data. Remote Sens. Environ. 79, 199–212.
Mishra, A.K., Singh, V.P., 2010. A review of drought concepts. J. Hydrol. (Amst.) 391, 202–216.
Niclòs, R., Galve, J.M., Valiente, J.A., Estrela, M.J., Coll, C., 2011. Accuracy assessment of land surface temperature retrievals from MSG2-SEVIRI data. Remote Sens. Environ. 115, 2126–2140.
Otkin, J.A., Anderson, M.C., Hain, C., Mladenova, I.E., Basara, J.B., Svoboda, M., 2013. Examining rapid onset drought development using the thermal infrared?based evaporative stress index. J. Hydrometeorol. 14, 1057–1074.
Rasmussen, M.O., Pinheiro, A.C., Proud, S.R., Sandholt, I., 2010. Modeling angular dependences in land surface temperatures from the SEVIRI instrument onboard the geostationary Meteosat Second Generation satellites. IEEE Trans. Geosci. Remote. Sens. 48, 3123–3133.
Rasmussen, M.O., Gottsche, F.-M., Olesen, F.-S., Sandholt, I., 2011. Directional effects on land surface temperature estimation from Meteosat Second Generation for savanna landscapes. IEEE Trans. Geosci. Remote. Sens. 49, 4458–4468.
Rhee, J., Im, J., Carbone, G.J., 2010. Monitoring agricultural drought for arid and humid regions using multi-sensor remote sensing data. Remote Sens. Environ. 114, 2875–2887.
Rouault, M., Richard, Y., 2003. Intensity and spatial extension of drought in South Africa at different time scales. Water SA 29, 489–500.
Sandholt, I., Rasmussen, K., Andersen, J., 2002. A simple interpretation of the surface temperature/vegetation index space for assessment of surface moisture status. Remote Sens. Environ. 79, 213–224.
Shang, H., Chen, L., Letu, H., Zhao, M., Li, S., Bao, S., 2017. Development of a daytime cloud and haze detection algorithm for Himawari-8 satellite measurements over central and eastern China. J. Geophys. Res. Atmos. 122, 3528–3543.
Shen, J., Huete, A., Tran, N.N., Devadas, R., Ma, X., Eamus, D., Yu, Q., 2018. Diverse sensitivity of winter crops over the growing season to climate and land surface temperature across the rainfed cropland-belt of eastern Australia. Agric. Ecosyst. Environ. 254, 99–110.
van Dijk, A., 2010. Landscape model (version 0.5) technical description. AWRA Technical Report Version 3. WIRADA/CSIRO Water for a Healthy Country Flagship, Canberra.
van Dijk, A., Renzullo, L.J., 2011. Water resource monitoring systems and the role of satellite observations. Hydrol. Earth Syst. Sci. 15, 39–55.
van Dijk, A.I.J.M., Beck, H.E., Crosbie, R.S., de Jeu, R.A.M., Liu, Y.Y., Podger, G.M., Timbal, B., Viney, N.R., 2013. The Millennium Drought in southeast Australia (2001–2009): natural and human causes and implications for water resources, ecosystems, economy, and society. Water Resour. Res. 49, 1040–1057.
Wan, Z., Dozier, J., 1996. A generalized split-window algorithm for retrieving land-surface temperature from space. IEEE Trans. Geosci. Remote. Sens. 34, 892–905.
Yang, Y., Anderson, M.C., Gao, F., Wardlow, B., Hain, C.R., Otkin, J.A., Alfieri, J., Yang, Y., Sun, L., Dulaney, W., 2018. Field-scale mapping of evaporative stress indicators of crop yield: an application over Mead, NE, USA. Remote Sens. Environ. 210, 387–402.
Zhang, A., Jia, G., 2013. Monitoring meteorological drought in semiarid regions using multi-sensor microwave remote sensing data. Remote Sens. Environ. 134, 12–23.
Zhang, X., Chen, N., Li, J., Chen, Z., Niyogi, D., 2017. Multi-sensor integrated framework and index for agricultural drought monitoring. Remote Sens. Environ. 188, 141–163.
Zhao, W., Li, Z.-L., 2013. Sensitivity study of soil moisture on the temporal evolution of surface temperature over bare surfaces. Int. J. Remote Sens. 34, 3314–3331.